Revista Mexicana de Astronomía y Astrofísica, **49**, 301–309 (2013)

PAHS AS TRACERS OF LOCAL AGN-STARBURST CONNECTION

Mario-A. Higuera-G.,[1] and Andrés F. Ramos P.[2]

Received 2012 November 22; accepted 2013 August 5

RESUMEN

El objetivo central de este trabajo fue investigar cómo procesos energéticos asociados a la actividad de los núcleos activos de galaxias están vinculados con aquellos que son debidos a la actividad de formación estelar nuclear y circunnuclear. Se usaron datos fotométricos y espectroscópicos con el fin de discriminar estos procesos en un conjunto de galaxias con brote de formación estelar, galaxias infrarrojas y AGNs. Se proponen nuevos diagramas de diagnóstico basados en la emisión de PAH en 7.7 μm, la razón entre la emisión en el infrarrojo medio y lejano L(MIR, FIR) y el parámetro q. Los diagramas de diagnóstico permiten comparar el comportamiento de los cuasares y galaxias Seyfert 1- Seyfert 2 con las galaxias con brote, y los LIRGs-ULIRGs.

ABSTRACT

The main purpose of this research was to investigate how energetic processes associated with active galactic nuclei (AGN) are related to those due to nuclear or circumnuclear star formation activity. Photometric and spectroscopic data were used to discriminate between these processes in a sample of starburst, infrared galaxies and AGNs. Here, we propose new diagnostic diagrams based on the 7.7 μm polycyclic aromatic hydrocarbon emission band, the L(MIR,FIR) infrared ratio and the q parameter. The diagnostic diagrams allow us to discriminate the behavior of quasars and Seyfert 1-Seyfert 2 galaxies from starbursts and LIRGs-ULIRGs objects.

Key Words: galaxies: active — galaxies: general — galaxies: nuclei

© Copyright 2013: Instituto de Astronomía, Universidad Nacional Autónoma de México

1. INTRODUCTION

Numerous studies (Cid Fernandez et al. 2001; Spoon et al. 2001; Imanishi 2006; Maiolino et al. 2007; Diamond-Stanic & Rike 2012), have made important contributions to quantify the star formation activity in several nuclear and circumnuclear regions of Active Galactic Nuclei (AGNs), and many diagnostic diagrams have been built in order to quantify the contribution of AGN and star formation to the IR luminosity. These diagrams use some bands of continuum and atomic emissions. The IR spectrum has many wavelengths that can be used to study the origin and connection between AGN activity and stellar processes (Clavel et al. 2000; Storchi-Bergmann et al. 2001; Imanishi & Wada 2004; Davies et al. 2007). The nuclear dust in AGNs is warmed up by the radiation of the central source, and also by the emissions coming from the ionized gas (Sanders & Mirabel 1996; Meléndez et al. 2008) and by those associated with stellar formation, the latter dominant in starburst and infrared type galaxies (Brand et al. 2006; Imanishi 2006).

Kennicutt (1998) and Panuzzo et al. (2003) carried out extensive research that resulted in a self-consistent set of estimates of rates of star formation along the Hubble sequence. These calibrations scale linearly with luminosity in two ranges of the continuum, ultraviolet and far infrared, as well as with emission lines such as Hα, Hβ, Pα, Pβ, Brα, Brγ and low probability of [O II] lines. These standard SFR indicators are often dominated by the AGN itself, particularly for unobscured (i.e., Type 1) sources. To mitigate this problem, Imanishi & Wada (2004), Schweitzer et al. (2006) and others use polycyclic aromatic hydrocarbons (PAHs) to trace star formation. The PAHs, radiating through IR fluorescence following vibrational excitation by a single ultraviolet (UV) photon, provide an indirect mea-

[1]Observatorio Astronómico Nacional, Facultad de Ciencias, Universidad Nacional de Colombia.

[2]Departamento de Física, Facultad de Ciencias, Universidad Nacional de Colombia.

TABLE 1

DATA FROM LITERATURE AND OUR ESTIMATIONS

Seyfert 1	log(L12/L60)	$L_{7.7\ \mu m}$ (W m^{-2})	$EQW_{7.7\ \mu m}$ (μm)	Flux(FIR) (W m^{-2})	$F_{1.4\ GHz}$ (W m^{-2} Hz^{-1})
NGC 863(Mrk590)	0.29	1.911E+38	0.067	3.43E-14	1.52E-28
NGC 3786(Mrk744)	−0.38	1.326E+38	0.489	7.68E-14	1.75E-28
NGC 4235	0.31	1.979E+37	0.110	1.86E-14	1.15E-28
NGC 4253(Mrk766)	−0.32	3.484E+38	0.231	1.90E-13	3.58E-28
NGC 5548	0.27	1.185E+38	0.054	5.51E-14	2.65E-28
Mrk817	−0.10	5.176E+38	0.061	9.75E-14	1.05E-28
NGC 7469	−0.58	3.497E+39	0.609	1.28E-12	1.70E-27
Mrk530(NGC 7603)	−0.03	1.020E+39	0.077	5.33E-14	2.29E-28
NGC 931(Mrk1040)	0.08	2.022E+38	0.050	1.41E-13	1.25E-28
Iras F03450+0055	0.47	2.177E+38	0.025	5.61E-14	3.05E-28
MCG-5-13-17	−0.10	2.085E+38	0.371	7.06E-14	1.33E-28
Mrk79	0.01	3.876E+38	0.068	7.85E-14	1.93E-28
NGC 2639	−0.40	2.905E+38	0.845	1.54E-13	1.08E-27
NGC 2992	−0.37	2.870E+38	0.496	4.05E-13	2.13E-27
UGC7064	−0.51	1.134E+39	0.781	1.60E-13	1.57E-28
MCG-2-33-34(NGC 4748)	−0.14	2.118E+38	0.448	6.57E-14	1.32E-28
IC4329A	0.42	2.541E+38	0.026	8.69E-14	6.24E-28
Mrk509	0.07	7.588E+38	0.071	6.34E-14	1.75E-28
Mrk478	0.02	1.127E+39	0.052	3.01E-14	4.89E-29
NGC 3227	−0.37	4.897E+37	0.309	4.87E-13	9.17E-28
Ark120	0.39	2.417E+38	0.011	3.45E-14	1.16E-28
NGC 4051	−0.22	1.094E+37	0.119	5.33E-13	8.87E-28
NGC 4593	−0.25	4.028E+37	0.033	1.74E-13	4.13E-29
Mrk279	−0.09	2.206E+38	0.034	6.87E-14	2.18E-28
NGC 526a	0.80	6.143E+37	0.017	1.83E-14	1.23E-28
NGC 3516	0.08	4.459E+37	0.048	8.57E-14	2.94E-28
NGC 4151	0.18	3.627E+37	0.049	3.22E-13	3.60E-27
Seyfert 2	log(L12/L60)	$L_{7.7\ \mu m}$ (W m^{-2})	$EQW_{7.7\ \mu m}$ (μm)	Flux(FIR) (W m^{-2})	$F_{1.4\ GHz}$ (W m^{-2} Hz^{-1})
Mrk334	−0.58	2.357E+39	0.6815	1.96E-13	2.62E-28
Mrk993	0.34	1.593E+37	0.126	2.64E-14	5.07E-29
Mrk573	0.06	2.489E+38	0.07205	5.13E-14	2.26E-28
NGC 1144	−0.58	9.577E+39	1.66	3.15E-13	1.45E-27
NGC 4388	−0.31	7.267E+38	0.406	5.60E-13	1.12E-27
NGC 5252	−0.67	2.135E+37	0.0209	7.44E-14	1.53E-28
NGC 5256(Mrk266SW)	-0.80	8.364E+39	1.64	3.78E-13	1.19E-27
NGC 5347	0.04	9.908E+37	0.134	7.94E-14	5.26E-29
NGC 5695	−0.02	5.655E+37	0.442	4.11E-14	5.92E-29
NGC 5929	−0.63	2.368E+37	0.4665	4.70E-13	1.02E-27
NGC 7674	−0.22	5.823E+39	0.304	2.84E-13	2.08E-27
NGC 7682	0.53	2.839E+37	0.2335	2.04E-14	5.62E-28
Mrk938	−0.92	6.217E+39	1.665	7.56E-13	6.29E-28
NGC 262(Mrk348)	0.08	3.701E+38	0.1045	6.15E-14	2.75E-27
NGC 513	−0.36	1.225E+39	0.675	1.14E-13	4.97E-28
F01475-0740	0.17	1.984E+38	0.14	4.23E-14	3.00E-27
NGC 1125	−0.59	4.087E+38	1.225	1.57E-13	5.45E-28
NGC 1320(Mrk607)	−0.11	3.196E+38	0.198	1.05E-13	5.64E-29
F04385-0828	−0.12	6.072E+38	0.07665	1.22E-13	1.79E-28
NGC 1667	−0.44	3.594E+39	3.16	3.79E-13	7.12E-28
NGC 3660	−0.29	6.660E+38	3.095	1.18E-13	1.16E-28
NGC 4501-S1-2	−0.43	3.549E+38	0.322	1.13E-12	2.79E-27
NGC 4968	−0.09	3.625E+38	0.285	1.14E-13	3.24E-28
MCG-3-34-64	−0.13	6.764E+38	1.61	2.61E-13	2.58E-27
NGC 5135	−0.72	3.521E+39	0.989	9.10E-13	1.88E-27
MCG-2-40-4	−0.27	1.714E+39	0.09725	2.01E-13	2.82E-28
NGC 7172	−0.41	5.551E+38	0.4245	3.41E-13	3.46E-28
MCG-3-58-7	−0.24	1.642E+39	0.0839	1.21E-13	1.17E-28
IC3639	−0.37	1.361E+39	0.717	3.79E-13	8.26E-28
Mrk34	−0.36	1.003E+39	0.1035	3.64E-14	1.79E-28
Mrk78	−0.23	9.051E+38	0.153	5.03E-14	3.43E-28
Mrk463	0.07	4.717E+39	0.06185	9.51E-14	3.58E-27
Mrk477	−0.3	8.556E+38	0.1435	6.59E-14	5.67E-28
NGC 1068	0.05	2.881E+39	0.1034	8.55E-12	4.56E-26
NGC 5033	−0.46	2.272E+38	1.315	1.00E-12	1.14E-27
IRAS 22377+0747	0.09	5.079E+38	0.2465	5.81E-14	1.42E-28
NGC 4579	−0.43	1.662E+37	0.04085	3.82E-13	9.10E-28
NGC 7314	−0.45	2.013E+37	0.209	3.00E-13	2.91E-28
NGC 1097	−0.65	1.187E+39	1.8	2.52E-12	2.34E-27
NGC 1386	−0.34	6.069E+37	0.2805	2.97E-13	3.49E-28
Mrk3	−0.02	4.356E+38	0.1395	1.65E-13	1.03E-26
NGC 3982	−0.41	2.164E+38	1.61	4.05E-13	5.30E-28
NGC 4507	−0.28	2.017E+38	0.04	2.08E-13	6.21E-28

© Copyright 2013: Instituto de Astronomía, Universidad Nacional Autónoma de México

TABLE 1 (CONTINUED)

Seyfert 2	log(L12/L60)	$L_{7.7\ \mu m}$ (W m^{-2})	$EQW_{7.7\ \mu m}$ (μm)	Flux(FIR) (W m^{-2})	$F_{1.4\ GHz}$ (W m^{-2} Hz^{-1})
NGC 5728	−0.83	3.584E+38	0.9385	4.50E-13	6.58E-28
NGC 5953	−0.57	9.253E+38	3.195	5.64E-13	8.59E-28
NGC 7592	−0.74	1.109E+40	1.655	3.82E-13	7.06E-28
NGC 4418 (NGC 4355)	−0.95	1.182E+39	8.19	1.83E-12	3.85E-28
LIRGs	log(L12/L60)	$L_{7.7\ \mu m}$ (W m^{-2})	$EQW_{7.7\ \mu m}$ (μm)	Flux(FIR) (W m^{-2})	$F_{1.4\ GHz}$ (W m^{-2} Hz^{-1})
NGC 6240	−0.92	1.467E+40	1.62	1.10E-12	4.01E-27
Iras23060+0505	−0.07	1.266E+40	0.02805	4.78E-14	6.30E-29
Iras20460+1925	0.11	5.326E+39	0.01167	6.33E-13	1.74E-28
NGC 253	−0.80	1.304E+38	5.85	3.78E-11	2.81E-26
NGC 828	−0.49	1.430E+40	2.455	6.42E-13	9.76E-28
Iras15250+3609	−0.86	2.200E+40	11.455	3.11E-13	1.36E-28
Iras17208-0014	−1.49	2.084E+40	3.765	1.45E-12	7.69E-28
Iras13126+2452	−1.60	2.889E+38	2.005	8.10E-13	2.89E-28
CGCG1510.8+0725	−1.66	8.913E+38	2.045	1.05E-12	4.79E-28
ULIRG-LINER	log(L12/L60)	$L_{7.7\ \mu m}$ (W m^{-2})	$EQW_{7.7\ \mu m}$ (μm)	Flux(FIR) (W m^{-2})	$F_{1.4\ GHz}$ (W m^{-2} Hz^{-1})
IRAS00188-0856	−0.64	2.592E+40	1.416	1.27E-13	1.48E-28
IRAS03250+1606	−0.44	1.842E+40	2.68	6.72E-14	8.93E-29
IRAS08572+3915	−0.67	6.346E+40	1.264	2.99E-13	4.09E-29
IRAS09039+0503	−0.63	1.563E+40	2.455	7.41E-14	5.83E-29
IRAS09116+0334	−0.38	8.951E+39	1.6455	5.84E-14	9.87E-29
IRAS09539+0857	−0.28	1.175E+41	12.425	5.99E-14	7.99E-29
IRAS10378+1108(9)	−0.62	1.868E+40	2.875	9.71E-14	7.89E-29
IRAS10485-1447	−0.5	1.828E+40	3.245	7.72E-14	3.90E-29
IRAS10494+4424	−0.77	1.605E+40	5.62	1.83E-13	1.99E-28
IRAS11095-0238	−1.03	5.148E+40	5.46	1.38E-13	2.36E-28
IRAS12112+0305	−1.15	1.583E+40	3.38	4.02E-13	2.19E-28
IRAS12127-1412	−0.37	2.240E+40	0.3505	6.43E-14	7.46E-28
IRAS12359-0725	−0.47	1.066E+40	1.285	5.73E-14	3.76E-29
IRAS14252-1550	−0.41	1.252E+40	1.535	6.08E-14	6.30E-29
IRAS14348-1447	−1.29	2.584E+40	3.225	3.12E-13	3.37E-28
IRAS15327+2340(Arp220)	−1.63	8.163E+39	7.52	4.78E-12	3.11E-27
IRAS16090-0139	−0.9	5.526E+40	2.34	1.79E-13	1.96E-28
IRAS16487+5447	−0.92	6.271E+39	2.98	1.32E-13	1.79E-28
IRAS17028+5817	−0.91	1.192E+40	4.435	1.28E-13	1.48E-28
IRAS17044+6720	−0.56	2.367E+40	0.308	5.40E-14	4.70E-29
IRAS21329-2346	−0.82	1.598E+40	2.405	8.16E-14	6.58E-29
ULIRG-HII	log(L12/L60)	$L_{7.7\ \mu m}$ (W m^{-2})	$EQW_{7.7\ \mu m}$ (μm)	Flux(FIR) (W m^{-2})	$F_{1.4\ GHz}$ (W m^{-2} Hz^{-1})
IRAS11387+4116	−0.23	1.237E+40	1.78	5.22E-14	6.11E-29
IRAS11506+1331	−0.71	3.430E+40	1.755	1.26E-13	1.27E-28
IRAS13539+2920	−0.61	1.698E+40	4.62	9.39E-14	1.09E-28
IRAS14060+2919	−0.51	2.337E+40	2.245	8.28E-14	8.74E-29
IRAS15206+3342	−0.65	2.699E+40	0.574	8.14E-14	1.01E-28
IRAS15225+2350	−0.57	1.852E+40	2.235	6.09E-14	6.20E-29
IRAS16474+3430	−0.54	1.019E+40	0.8125	110E-13	1.04E-28
IRAS21208-0519	−0.41	1.144E+40	3.595	5.90E-14	6.01E-29
ULIRG-Seyfert 1	log(L12/L60)	$L_{7.7\ \mu m}$ (W m^{-2})	$EQW_{7.7\ \mu m}$ (μm)	Flux(FIR) (W m^{-2})	$F_{1.4\ GHz}$ (W m^{-2} Hz^{-1})
IRAS01572+0009(Mrk1014)	−0.57	8.698E+39	0.0612	9.94E-14	2.46E-28
IRAS12265+0219(3C273)	0.13	1.363E+39	0.00352	1.03E-13	5.17E-25
IRAS12540+5708(Mrk231)	−0.53	1.436E+40	0.08665	1.42E-12	2.90E-27
IRAS15462-0450	−0.77	1.058E+40	0.189	1.33E-13	1.20E-28
ULIRG-Seyfert 2	log(L12/L60)	$L_{7.7\ \mu m}$ (W m^{-2})	$EQW_{7.7\ \mu m}$ (μm)	Flux(FIR) (W m^{-2})	$F_{1.4\ GHz}$ (W m^{-2} Hz^{-1})
IRAS05189-2524	−0.57	8.346E+39	0.16	5.88E-13	2.71E-28
IRAS08559+1053	−0.35	2.513E+40	0.5465	6.10E-14	1.15E-28
IRAS13428+5608(Mrk273)	−1.26	1.101E+40	1.59	9.76E-13	1.36E-27
IRAS13451+1232(PKS1345+12)	−0.44	3.343E+39	0.0538	8.84E-14	5.07E-26
IRAS17179+5444	−0.53	9.085E+39	0.239	6.83E-14	3.12E-27
Starburst	log(L12/L60)	$L_{7.7\ \mu m}$ (W m^{-2})	$EQW_{7.7\ \mu m}$ (μm)	Flux(FIR) (W m^{-2})	$F_{1.4\ GHz}$ (W m^{-2} Hz^{-1})
IC 342	−0.38	1.488E+36	1.98	1.08E-11	1.79E-27
Mrk52	−0.53	1.166E+38	0.8375	2.25E-13	1.23E-28
NGC 0520	−0.85	3.895E+39	2.655	1.62E-12	1.66E-27
NGC 1222	−0.72	4.933E+38	2.03	6.19E-13	5.80E-28
NGC 1365	−0.57	5.022E+38	0.4115	5.15E-12	3.53E-27
NGC 2146	−0.63	7.437E+38	4	7.21E-12	1.01E-26
NGC 2623	−1.35	4.323E+39	2.43	1.10E-12	8.99E-28
NGC 3310	−0.65	9.577E+37	1.81	1.68E-12	3.41E-27
NGC 3556	−0.45	2.910E+37	2.815	2.03E-12	2.03E-27
NGC 3628	−0.54	2.434E+38	7.485	3.11E-12	2.73E-27

© Copyright 2013: Instituto de Astronomía, Universidad Nacional Autónoma de México

TABLE 1 (CONTINUED)

Starburst	log(L12/L60)	$L_{7.7\ \mu m}$ (W m^{-2})	$EQW_{7.7\ \mu m}$ (μm)	Flux(FIR) (W m^{-2})	$F_{1.4\ GHz}$ (W m^{-2} Hz^{-1})
NGC 4194	−0.67	1.484E+39	1.935	1.07E-12	9.46E-28
NGC 4676	−0.69	3.494E+39	3.325	1.52E-13	2.46E-28
NGC 4818	−0.62	1.970E+38	0.892	9.89E-13	4.28E-28
NGC 7252	−0.52	3.191E+39	1.92	2.18E-13	2.31E-28
NGC 7714	−0.68	7.515E+38	1.17	5.17E-13	6.18E-28
NGC 1614	−0.67	4.715E+39	1.945	1.48E-12	1.29E-27
QSOS-QUASARs PG	log(L12/L60)	$L_{7.7\ \mu m}$ (W m^{-2})	$EQW_{7.7\ \mu m}$ (μm)	Flux(FIR) (W m^{-2})	$F_{1.4\ GHz}$ (W m^{-2} Hz^{-1})
PG1229+204(Mrk771)	0.34	3.182E+38	0.02285	*1.18E-14*	*2.63E-29*
PG1302-102	0.24	1.590E+40	0.08765	*1.55E-14*	*6.68E-27*
PG1426+015	0.28	6.972E+38	0.01223	*1.53E-14*	*2.54E-29*
PG2349-014	0.28	3.045E+39	0.0862	*1.25E-14*	*1.51E-26*
PG0007+106	0.37	9.131E+38	0.02015	*1.76E-14*	*9.19E-28*
PG1115+407	0.51	4.891E+39	0.122	*8.92E-15*	*9.68E-30*
PG1119+120	0.11	4.083E+38	0.02525	*2.49E-14*	*2.82E-29*
PG1351+640	−0.01	3.979E+39	0.3965	3.76E-14	3.07E-28
PG1404+226	0.52	1.449E+38	0.0219	*9.38E-15*	*2.63E-29*
PG1448+273	0.48	4.580E+38	0.033065	*6.98E-15*	*2.82E-29*
PG1534+580	0.46	1.280E+38	0.03	*1.29E-14*	*4.51E-29*
PG1612+261	0.37	1.496E+39	0.0287	*1.14E-14*	*1.68E-28*
PG1613+658(Mrk876)	−0.14	4.017E+39	0.03245	2.96E-14	3.66E-29
PG2130+099	0.24	1.102E+39	0.02375	2.50E-14	5.64E-29
QSOS-QUASAR 3CR	log(L12/L60)	$L_{7.7\ \mu m}$ (W m^{-2})	$EQW_{7.7\ \mu m}$ (μm)	Flux(FIR) (W m^{-2})	$F_{1.4\ GHz}$ (W m^{-2} Hz^{-1})
3C48	−0.34	4.006E+40	0.0522	*3.85E-14*	*1.51E-25*
3C65	0.55	1.053E+41	0.10945	*2.52E-15*	*2.92E-26*
3C79	−0.09	7.999E+39	0.07533	*8.84E-15*	*4.57E-26*
3C84	−0.13	9.167E+36	0.00122	3.20E-13	2.15E-25
3C249.1	0.14	3.180E+37	0.000257	*3.05E-15*	*2.20E-26*
3C270	1.05	4.527E+36	0.06	4.49E-15	1.66E-25
3C272.1	0.22	8.945E+35	0.0302	2.87E-14	5.70E-26
3C274	0.75	2.825E+36	0.055	1.78E-14	1.30E-24
3C293	−0.19	2.055E+39	0.688	1.56E-14	3.84E-26
3C303.1	0.1	1.317E+39	0.12005	*6.53E-15*	*1.77E-26*
3C323.1	0.49	2.553E+39	0.0344	*3.40E-15*	*2.25E-26*
3C330	0.08	7.048E+39	0.1064	*8.91E-15*	*6.57E-26*
3C381	0.28	1.071E+39	0.03238	*3.66E-15*	*3.79E-26*
3C382	0.53	1.928E+38	0.0126	*7.32E-15*	*5.16E-26*
3C386	0.55	1.637E+36	0.0195	*3.34E-15*	*6.54E-26*
3C445	0.53	3.817E+38	0.0171	*2.29E-14*	*5.79E-26*

The data in italic text show upper limits.

© Copyright 2013: Instituto de Astronomía, Universidad Nacional Autónoma de México

surement of the UV radiation field strength from stars (Peeters 2002; Diamond-Stanic & Rike 2012). However, high-energy photons or shocks linked with AGN may destroy or modify their molecular carriers (Yong et al. 2007). Recently, Maiolino et al. (2007) and Diamond-Stanic & Rike (2012) introduced two other calibrations for the rate of star formation using 7.7 μm, and 11.3 μm polycyclic aromatic hydrocarbon (PAH) luminosities, respectively.

In this paper, we describe the estimation of an MIR-FIR indicator, and calculate the q parameter in order to construct two new diagnostic diagrams.

2. THE SAMPLE AND SOURCES

The galaxy data collected for this work are summarize in Table 1. As shown in this table, the sample is heterogeneous and came from different instruments: the IR continuum from the IRAS satellite, the radio continuum from NRAO, and the PAHs bands extracted by us from the Spitzer database. The galaxies have a redshift range between 0.001878 and 0.55. The mid-infrarred and far-infrarred observations at 12, 25, 60 and 100 μm, came from a sub sample of the complete list of objects contained in the IRAS Revised Bright Galaxy Sample (RBGS), a flux- limited sample of all extragalactic objects brighter than 5.24 Jy at 60 μm, covering the entire sky surveyed by the Infrared Astronomical Satellite. These data are condensed in IRAS catalogues (Neugebauer et al. 1984; Soifer et al. 1989; Moshir et al. 1990; Huchra & Burg 1992; Rush, Malkan, & Spinoglio 1993; Sanders et al. 2003). The samples are not expected to be biased by the presence of nuclear starburst (Imanishi 2003; Imanishi & Wada 2004). For the same subsample of IR objects, we selected corrected flux densities of 1.4 GHz, from the complete NRAO VLA Sky Survey (NVSS) (Condon 1992; Condon et al. 1998). The NVSS contains the majority of galaxies in the IRAS Faint Source Catalog. Finally, the PAH measurements were extracted

© Copyright 2013: Instituto de Astronomía, Universidad Nacional Autónoma de México

from Spitzer satellite observations. These observations use the data (BCD) of the Spitzer Heritage Archive (SHA) using 5.3–14 μm (SL) and 14–40 μm (LL) low resolution ($R \sim 100$) modules with widths of $\sim$3.7″ and 10.5″ respectively. The data were extracted using three algorithms in the IDL environment: CUBISM, a method for reconstructing spectral cubes using the BCD default spectral images, IRSCLEAN, which creates a mask of damaged pixels from the BCD data set, and PAHFIT, an algorithm for the decomposition of the MIR spectrum, which focuses on the overall behavior of PAH emissions relative to its underlying continuum (Smith et al. 2007a,b).

The sample consists of one subsample composed of typical IR emission galaxies: 14 (9) LIRGs selected from Imanishi, Dudley, & Maloney (2006) and Imanishi (2006); 24 (21) ULIRGs-LINER, 12 (8) ULIRGs-HII, 7 (4) ULIRGs-Sy1 y 7 (5) ULIRGs-Sy2, published by Imanishi (2006) and Imanishi et al. (2007); 20 (16) starburst galaxies published by Brand et al. (2006), and a second subsample of AGNs composed of 41 (27) Seyfert 1 and 53 (47) Seyfert 2 galaxies published by Imanishi (2003), Imanishi & Wada (2004), Rodríguez-Ardila & Viegas (2003), Rush et al. (1993), Huchra & Burg (1992) and Clavel et al. (2000); 108 (14) PG and 93 (16) 3CR quasars and QSOs taken from the work of Schweitzer et al. (2006) and Yong et al. (2007). The values in parentheses show the galaxies extracted by us in order to get the PAH features. The information was complemented with data selected from the NASA/IPAC Extragalactic Database-NED, the Simbad-VizieR database and 2MASS. Although not all the samples are statistically complete, the subsamples provide useful information about the behavior and particularities of the different types of galaxies selected for this work, and major conclusions can be obtained.

3. THE MIR-FIR INDICATOR

It is well known that the emission continuum in the near-, mid- and far-infrared spectra, represents different temperature states of molecular clouds and their possible origins (AGN or stellar activity). For this reason, we define the measure $L(12,60)$ in order to find differences between the emissions in the MIR and FIR, following a criterion similar to that adopted by Murayama, Mouri, & Taniguchi (2000),

$$L(12,60) = \log\left[\frac{L(12\ \mu\mathrm{m})}{L(60\ \mu\mathrm{m})}\right]. \qquad (1)$$

The $L(12.60)$ values for quasars and Seyfert 1 galaxies, here grouped together under the label *Type 1*, lie in the range -0.63 to 1.05. For all Seyfert 2 galaxies, the values lie between -0.92 and 0.53, while for the other set of galaxies: starburst, LIRGs and ULIRGs, the values lie in the range -1.63 and 0.5.

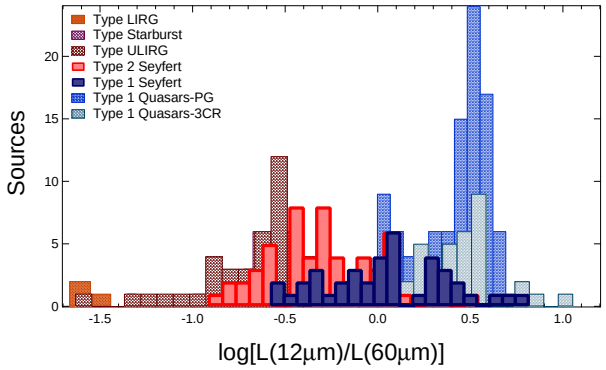

Fig. 1. $L(12,60)$ histogram plot for all galaxies included in the analysis. The Seyfert 1 galaxies and quasars are well differentiated from the Seyfert 2, starburst, LIRG and ULIRG galaxies. The color figure can be viewed online.

The separation between *Type 1* objects and the ULIRG-LIRG-Starburst galaxies, also observed in Seyfert 1 and 2 galaxies (Figure 1), is consistent with the fact that emissions in the near- and mid-infrared (NIR-MIR) spectra from the dust heated by the AGN, are dominant in *Type 1* objects. In order to explore this behavior, we applied the Kolmogorov-Smirnov (KS) test to *Type 1* objects and Seyfert 2 galaxies, and the results are shown in Table 2. The P-values for $L(12\ \mu\mathrm{m})$, $L(60\ \mu\mathrm{m})$ and $L(12\ \mu\mathrm{m})/L(60\ \mu\mathrm{m})$ reject the null hypothesis, showing significant differences between the mid-IR and far-IR emissions. For the 7.7 μm-PAH emissions the test also rejects the null hypothesis, i.e., there is no isotropy in the PAH emissions. Considering the latter as a tracer of the existence of star formation activity, the KS test provides statistical validation for the observed differences in our sample.

The anisotropies found in the KS test have two possible explanations: either the PAH bands are diluted by intense X-ray emissions (Yong et al. 2007) (a1), or different stages of stellar activity are present in active galactic nuclei (a2). These two alternatives will be discussed in the following sections.

In order to separate the sample of galaxies by their degree of nuclear activity as well as to assess the contribution associated with star formation, we selected the $L(12,60)$ ratio and the 7.7 μm PAH equivalent width for the construction of a new diagnostic diagram (Figure 2). *Type 1* objects occupy the top half of the diagram, while the bottom half

TABLE 2

K-S TEST DONE OVER *TYPE 1* AND SEYFERT 2 GALAXIES.

K-S Test	$\log[L(12\ \mu\text{m})]$	$\log[L(60\ \mu\text{m})]$	$\log[L(12,60)]$	$\log[L(7.7\ \mu\text{m})]$
α	0.05	0.05	0.05	0.05
Type 1	169	169	169	57
Sy2	53	53	53	47
D	0.681925	1	0.975215	0.574095
Critical	0.228102	0.228102	0.228102	0.283724
p-value	1.9598E-17	5.30404E-37	5.2752E-35	1.306E-8
Result	Reject	Reject	Reject	Reject

© Copyright 2013: Instituto de Astronomía, Universidad Nacional Autónoma de México

is mainly occupied by Seyfert 2, starburst galaxies, LIRGs and ULIRGs. This pattern is due to differences in the observed emissions at 12 μm and 60 μm. At higher values of L(12,60), the dust is heated by the active nucleus and produces a warm black body emission (Pope et al. 2008), while at intermediate values of the ratio, the molecular clouds are heated by AGN and stellar activity. At lower values of L(12,60) the star component heats the dust at temperatures between 30–50 K (Hass et al. 2003). The lowest L(12,60) value, associated with the quasar PG 1049-005, separates *Type 1* from the rest of the sample (Figure 2) and is equal to the separation value between Seyfert 1 and Seyfert 2 galaxies (-0.6), derived by Murayama et al. (2000).

The dotted vertical lines shown in Figure 2 correspond to the regions defined by Spoon et al. (2007), but in our diagram, Classes 1A-2A are occupied by unobscured AGNs, Classes 1B-2B by composite (AGN/SB activity) galaxies and Class 2C mainly by starburst galaxies. The square box located in the lower right quadrant delimits a particular region denominated by us as *Active star formation region* (ASFR). In the ASFR are located 78% of LINERs and all starburst and ULIRGs galaxies. Moreover, 43% of the Seyfert 2, and 11% of Seyfert 1 samples are also present.

In the ASFR appear the LINERs: NGC 1097 (not labeled in Figure 2) and NGC 253. NGC 1097 is a galaxy with a relatively young stellar population ($\sim 10^6$ years), at a distance less than 9 pc from the nucleus (Storchi-Bergmann et al. 2005; Prieto, Maciejewski, & Reunanen 2005), which is the source of dust heating (Mason et al. 2007); NGC 253 is a galaxy in which a strong starburst and a weak AGN coexist (Müller-Sánchez et al. 2010). The particular position of NGC 1097 and NGC 253 within the ULIRGs and starburst galaxies in the diagram, validates star formation as the cause of dust heating, and minimizes the role of the active nucleus. Also in this region appears the Seyfert 1 galaxy, NGC 3227 (just in the upper limit of the ASFR frame); Davis et al. (2007) resolved the nuclear stellar distribution of this galaxy and found that within a few parsecs of the AGN there was an intense starburst, the most recent episode of which began $\sim$40 Myr ago, but has now ceased. In the lower half of the ASFR, two interacting systems appear, NGC 2623 and ULIRG-LINER Arp 220. The first is a triple system with intense star formation, superluminal in the infrared, and extremely bright in radio (Read & Ponman 1998). The second is the most luminous object in the IRAS catalogue, also classified as "heavily extinguished starburst" by Hatziminaoglou et al. (2008), and localized in the region 3B of the Spoon (2007) diagram, an area in which absorption is the dominant factor.

The diagram of Figure 2 is an original contribution to this field; it separates the sample in two groups of objects, one consisting of starburst-ULIRGs (ASFR region) and the other of *Type 1*-Seyfert 2 galaxies. In the ULIRG-starburst group, the stellar component is the factor responsible for warming the dust, which is reflected in the smaller values for L(12,60), and the values of PAH 7.7 μm (ASFR zone). The fact that some Seyfert galaxies with star formation appear in this area, confirms the usefulness of the diagram to validate the existence of star activity in AGNs. Additionally this diagram complements the Spoon (2007) diagram with new data from IRAS observations and our measurements of PAH in 7.7 μm. Finally, our spectra extraction, using the PAHFIT tool and adjusting for every object the continuum, solves the overestimation in the 7.7 μm PAH equivalent width shown by Clavel et al. (2000).

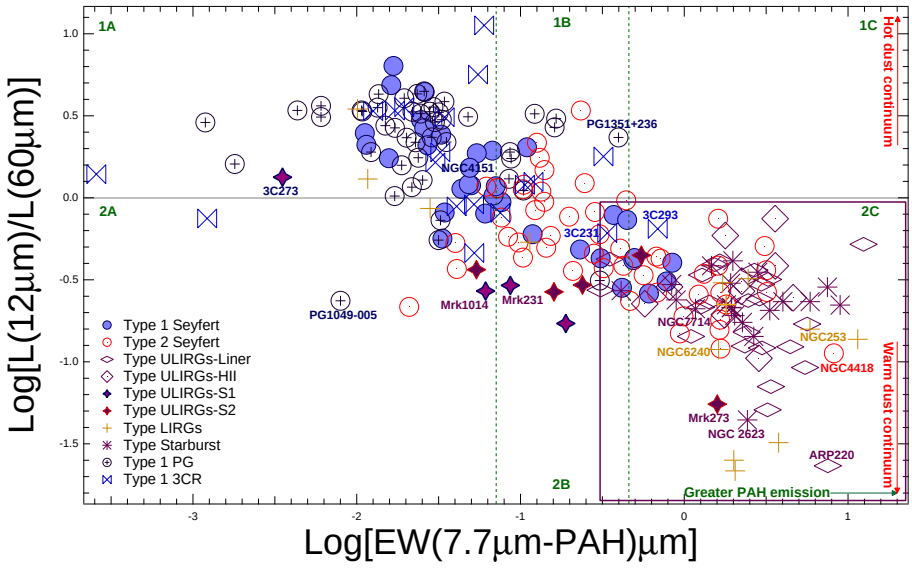

Fig. 2. Diagnostic plot of the $L(12\ \mu\mathrm{m})/L(60\ \mu\mathrm{m})$ luminosity ratio as a function of the 7.7 μm PAH equivalent width. The sample has a redshift z between 0.000103, for the starburst IC 342, and 0.55 for the radio source 3C330. The violet square box, at the right, defines the *ASFR* region. The color figure can be viewed online.

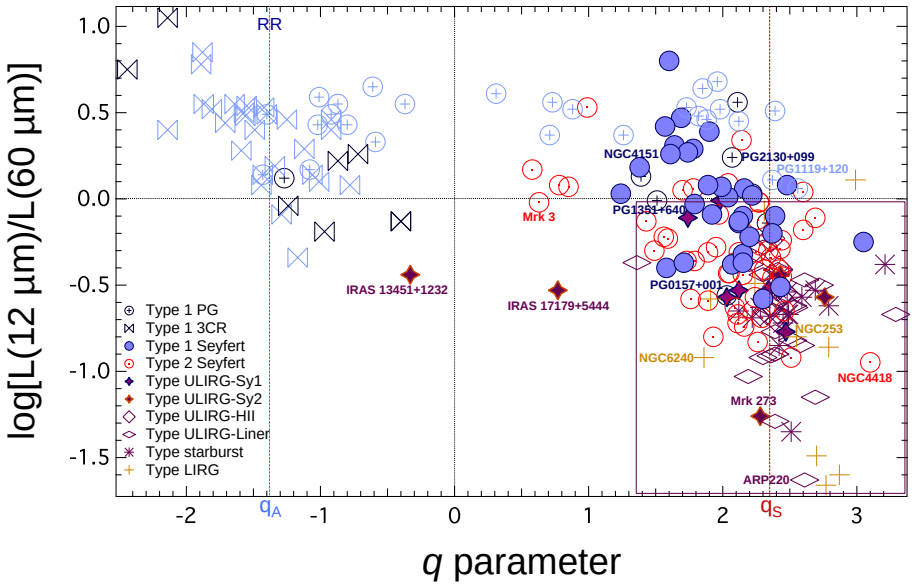

Fig. 3. L(12,60) indicator plotted against the q parameter. The red dotted line marked with the label q_S shows the value 2.35 (Sanders & Mirabel 1996) for starburst galaxies. The light blue symbols represent quasars with upper limit estimations. The blue dotted line labeled q_A (-1.38) represents the mean of all values $q < 0$. The graphic includes additional sources from Schweitzer et al. (2006) and Yong et al. (2007). The color figure can be viewed online.

4. THE FIR-RADIO CORRELATION

The infrared emissions are largely due to the reemission of dust heated by massive stars, while supernova explosions of massive young stars are the source of radio emissions (de Jong et al. 1985). A quantifier of stellar activity is the slope of the correlation between radio emission and far-infrared emission or q parameter (Helou, Soifer, & Rowan-Robinson 1985; Condon 1992),

$$q \equiv \log \frac{F_{\mathrm{FIR}}/(3.75 \times 10^{12}\ \mathrm{Hz})}{F_{\nu}(1.4\ \mathrm{GHz})(\mathrm{W\ m^{-2}\ Hz^{-1}})}\,, \qquad (2)$$

© Copyright 2013: Instituto de Astronomía, Universidad Nacional Autónoma de México

where F_ν (1.4 GHz) is the flux density at 1.4 GHz, and $F_{\rm FIR}$ is the far infrared flux calculated as,

$$\mathrm{FIR} \equiv 1.26\times10^{-14}(2.58F_{60\ \mu\mathrm{m}} + F_{100\ \mu m})\ \mathrm{W\ m^{-2}}, \quad (3)$$

where $F_{60\ \mu\mathrm{m}}$ and $F_{100\ \mu\mathrm{m}}$ are the IRAS 60 μm and 100 μm band flux densities measured in Janskys (Jy).

At low IR luminosities, the average value of q tends to increase from younger to older stellar populations (Condon 1992; Xu, Lisenfeld, & Volk 1994). Sanders & Mirabel (1996) established, using IRAS observations, a q value equal to 2.35 for objects with intense star formation, and Sabater et al. (2008) used a FIR, F(1.4Ghz) correlation to identify galaxies with excess radio emission as AGN candidates.

In this context, the q parameter is also a discriminator between sources that have strong star formation and those (AGNs) in which the radio luminosity is greater than the value predicted by the radio-FIR correlation (Yun, Reddy, & Condon 2001). Therefore, we conducted a review of the q parameter for our sample. Figure 3 shows the graph of the L(12,60) indicator as a function of the q parameter. Following the distribution of the sample along the vertical axis a frame is drawn, indicating the *Active star formation region* area. The dotted lines at the origin separate the sample by the dominant emission. On the vertical axis, the sources are discriminated according to emission intensity, between mid-infrared and cold dust (60 μm). On the horizontal axis, the objects are separated into those with strong radio emission (left) and those with dominance in the far-infrared emission (right). The dashed line labeled $q_{\rm s}$ shows the value determined by Sanders & Mirabel (1996).

In Figure 3, three QSOs: PG 1351+640, PG 1119+120 and PG 2130+099 lie in the region with positive q parameter. Farrah et al. (2009) also discuss these three sources and suggest that they represent the last part of an evolutionary sequence, post-IR, where the contribution of star formation falls to mid-infrared, at the expense of increasing the contribution of the AGN. However, as the diagram also shows, a large sample of galaxies lie in the region associated with q parameter values <0, here called: *Radio Region* (RR). In radio galaxies, the accretion onto massive black holes located in giant ellipticals is less than $10^{-3}\ M_\odot\ \mathrm{yr}^{-1}$, and this condition restricts star formation activity (Dicken et al. 2011). In addition, radio jets ionize the gas, cooling it and reducing the activity of star formation and dust heating (Ramos Almeida 2009). This graph is particularly suitable for discriminating highly noisy radio galaxies with low density material from those with intense FIR emissions associated with dense clouds. The sources located in the radio region RR are not directly linked to the evolutionary scenarios presented in the literature. Whether or not they are a final stage of an evolutionary scenario is an open question. However, the graph confirms that they are active nuclei with low stellar activity.

5. CONCLUSIONS

The diagnostic diagram, in which L(12,60) is plotted against the equivalent width of the 7.7 μm PAH emission, is an original tool for discriminating galaxies by strength and source of activity (AGN or star formation). The ULIRG-starburst galaxies concentrate in the ASFR region, verifying that the stellar component is the dominant factor responsible for the heating of dust, while, for the remaining galaxies, the AGN component is dominant.

The galaxies sampled in this study overlap with the sampling of previous authors (Storchi-Bergmann et al. 2001; Haas et al. 2003; Koulouridis et al. 2006; Farrah et al. 2009), even though each study used different variables. Nevertheless, in all of our studies, including this one, the distribution of galaxies in the parameter space is similar, and this demonstrates the discriminatory power of our method. The relative position of NGC 253, a weak AGN, on the right side, NGC 1027, a LINER, in the middle and NGC 3227, a Seyfert 1, on the left side of the ASFR region, validates the coexistence of star formation and an active nucleus.

The diagnostic diagram of L(12,60) vs q parameter validates the relationship between the far-infrared emission and the emission at 1.4 GHz (associated with supernova-type events) that holds for galaxy type starbursts, ULIRGs and LIRGs. The strong 1.4 GHz emission from an active nucleus defines a new region with negative q values (region RR) where 3CR radio sources, some of the quasars (PG) and a ULIRG-SY2 are located. There, the stellar activity for radio galaxies is lower. This diagram, like the previous one, is useful for the identification of objects, according to their level of nuclear activity, in large observational surveys.

The scenarios (a1) and (a2), proposed in § 3, coexist in the diagnostic diagrams. The dominant activity in a galaxy determines the predominance of one or the other scenario and its relative location in one of the evolutionary sequences suggested by Storchi-Bergmann et al. (2001), Haas et al. (2003), Farrah et al. (2009).

© Copyright 2013: Instituto de Astronomía, Universidad Nacional Autónoma de México

The authors wish to thank the anonymous reviewer for his/her very careful reading of the manuscript and for very important and fruitful comments and suggestions. We also thank Alberto Rodríguez Ardila for useful and fundamental discussions, and Lauren Raz for her English style suggestions.

REFERENCES

Brandl, B., et al. 2006, ApJ, 653, 1129
Cid Fernandes, R., Heckman, T., Schmitt, H., González Delgado, R. M., & Storchi-Bergmann, T. 2001, ApJ, 558, 81
Clavel, J., et al. 2000, A&A, 357, 839
Condon, J. 1992, ARA&A, 30, 575
Condon, J. J., Cotton, W. D., Greisen, E. W., Yin, Q. F., Perley, R. A., Taylor, G. B., & Broderick, J. J. 1998, AJ, 115, 1693
Diamond-Stanic, A. M., & Rieke, G. H. 2012, ApJ, 746, 168
Davies, R. I., Müller-Sánchez, F., Genzel, R., Tacconi, L. J., Hicks, E. K. S., Friedrich, S., & Sternberg, A. 2007, ApJ, 671, 1388
de Jong, T., Klein, U., Wielebinsky, R., & Wunderlich, E. 1985, A&A, 147, L6
Dicken, D., et al. 2011, arXiv:1111.4476v2
Farrah, D., et al. 2009, ApJ, 700, 395
Haas, M., et al. 2003, A&A, 402, 87
Hatziminaoglou, E., et al. 2008, MNRAS, 386, 1252
Helou, G., Soifer, B. T., & Rowan-Robinson, M. 1985, ApJ, 298, L7
Huchra, J., & Burg, R. 1992, ApJ, 393, 90
Imanishi, M. 2003, ApJ, 599, 918
_____. 2006, AJ, 131, 2406
Imanishi, M., Dudley, C., Maiolino, R., Maloney, P., Nakagawa, T., & Risaliti, G. 2007, ApJS, 171, 72
Imanishi, M., Dudley, C., & Maloney, P. 2006, ApJ, 637, 114
Imanishi, M., & Wada, K. 2004, ApJ, 617, 214
Kennicutt, R. 1998, ARA&A, 36, 189
Koulouridis, E., Chavushyan, V., Plionis, M., Krongold, Y., & Dultzin-Hacyan, D. 2006, ApJ, 651, 93
Maiolino, R., Shemmer, O., Imanishi, M., Netzer, H., Oliva, E., Lutz, D., & Sturm, E. 2007, A&A, 468, 979
Mason, R., Levenson, N. A., Packham, C., Elitzur, M., Radomski, J., Petric, A. O., & Wright, G. S. 2007, ApJ, 659, 241
Meléndez, M., Kraemer, S. B., Schmitt, H. R., Crenshaw, D. M., Deo, R. P., Mushotzky, R. F., & Bruhweiler, F. C. 2008, ApJ, 689, 95
Moshir, M., et al. 1990, Bull. Am. Astron. Soc., 22, 1325
Müller-Sánchez, F., González-Martín, O., Fernández-Ontiveros, J. A., Acosta-Pulido, J. A., & Prieto, M. A. 2010, ApJ, 716, 1166
Murayama, T., Mouri, H., & Taniguchi, Y. 2000, ApJ, 528, 179
Neugebauer, G., et al. 1984, ApJ, 278, L1
Panuzzo, P., Bressan, A., Granato, G. L., Silva, L., & Danese, L. 2003, A&A, 409, 99
Peeters, E. 2002, Polycyclic Aromatic Hydrocarbons and Dust in Regions of Massive Star Formation (Groningen: Univ. of Groningen)
Pope, A., et al. 2008, ApJ, 675, 1171
Prieto, M. A., Maciejewski, W., & Reunanen, J. 2005, AJ, 130, 1472
Ramos Almeida, C. 2009, Thesis, Instituto de Astrofísica de Canarias, Universidad de La Laguna
Read, A. M., & Ponman, T. J. 1998, MNRAS, 297, 143
Rodríguez-Ardila, A., & Viegas, S. M. 2003, MNRAS, 340, L33
Rush, B., Malkan, M. A., & Spinoglio, L. 1993, ApJS, 89, 1
Sabater, J., Leon, S., Verdes-Montenegro, L., Lisenfeld, U., Sulentic, J., & Verley, S. 2008, A&A, 486, 73
Sanders, D. B., Mazzarella, J. M., Kim, D. C., Surace, J. A., & Soifer, B. T. 2003, AJ, 126, 1607
Sanders, D. B., & Mirabel, I. F. 1996, ARA&A, 34, 749
Schweitzer, M., et al. 2006, ApJ, 649, 79
Smith, J. D. T., et al. 2007a, PASP, 119, 1133
Smith, J. D. T., et al. 2007b, ApJ, 656, 770
Soifer, B. T., Boehmer, L., Neugebauer, G., & Sanders, D. B. 1989, AJ, 98, 766
Spoon, H., Keane, J., Tielens, A., Lutz, D., & Moorwood, A. 2001, A&A, 365, L353
Spoon, H., et al. 2007, ApJ, 654, L49
Storchi-Bergmann, T., González Delgado, R., Schmitt, H., Cid Fernandes, R., & Heckman, T. 2001, ApJ, 559, 147
Storchi-Bergmann, T., Nemmen, R. S., Spinelli, P. F., Eracleous, M., Wilson, A. S., Filippenko, A. V., & Livio, M. 2005, ApJ, 624, L13
Xu, C., Lisenfeld, U., & Volk, H. J. 1994, A&A, 285, 19
Yong, S., et al. 2007, ApJ, 669, 841
Yun, M. S., Reddy, N. A., & Condon, J. J. 2001, ApJ, 554, 803

Mario Armando Higuera Garzón: Observatorio Astronómico Nacional, Facultad de Ciencias, Universidad Nacional de Colombia, Bogotá, Colombia (mahiguerag@unal.edu.co).
Andrés Felipe Ramos Padilla: Departamento de Física, Facultad de Ciencias, Universidad Nacional de Colombia, Bogotá, Colombia (aframosp@unal.edu.co).

© Copyright 2013: Instituto de Astronomía, Universidad Nacional Autónoma de México